iScience

CellPress
OPEN ACCESS

Article

Impact of gadolinium doping into the frustrated antiferromagnetic lithium manganese oxide spinel

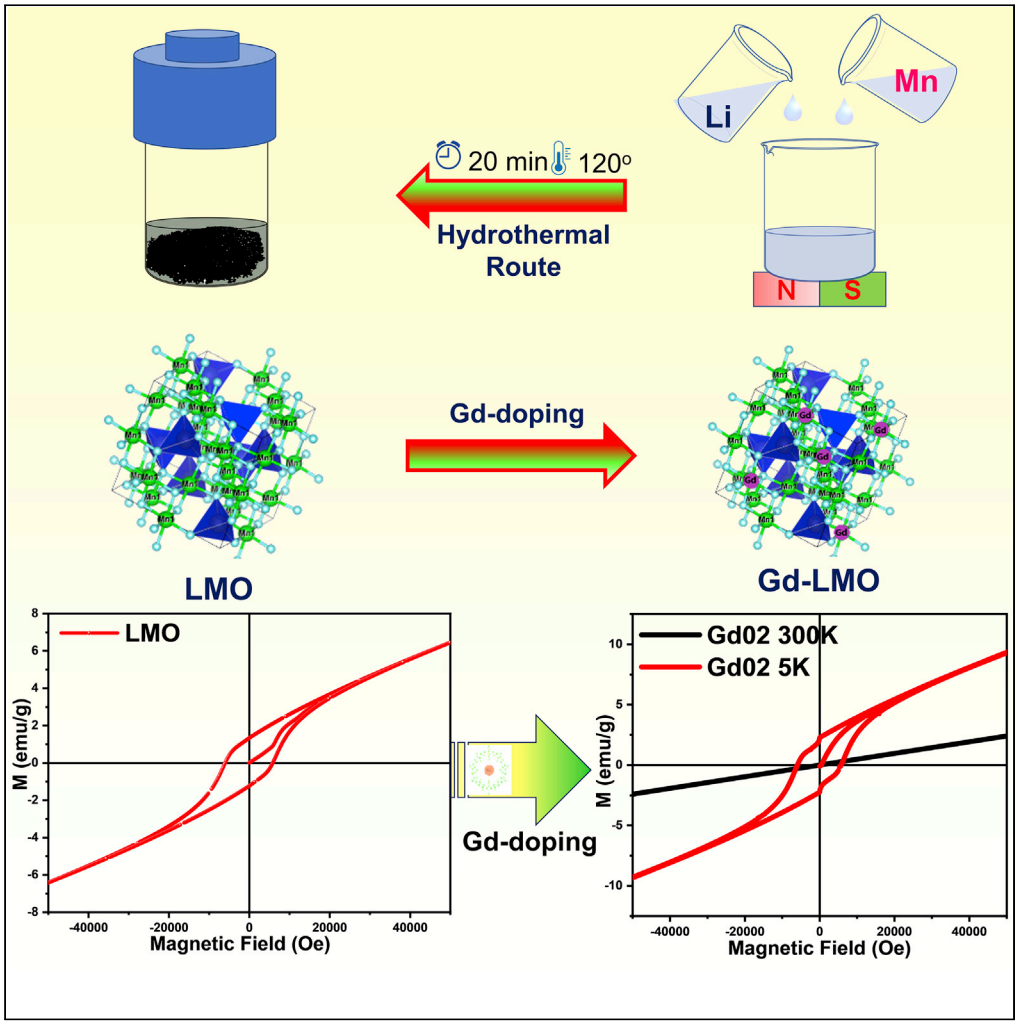

Bhagirath Saini, R. Krishnapriya, Devika Laishram, Manoj K. Singh, Rahul Singhal, Sateesh Bandaru, Rakesh K. Sharma

sbandaru@hdu.edu.cn (S.B.)
rks@iitj.ac.in (R.K.S.)

Highlights

Synthesis of Gd-doped LMO via sol-gel method

Correlation of magnetic properties with Raman spectroscopy and DFT calculations

The combined effect of Mn^{3+}-Mn^{3+} interaction with 3d-4f election spin coupling

Saini et al., iScience 26, 105869
January 20, 2023
https://doi.org/10.1016/j.isci.2022.105869

iScience

CellPress
OPEN ACCESS

Article

Impact of gadolinium doping into the frustrated antiferromagnetic lithium manganese oxide spinel

Bhagirath Saini,[1] R. Krishnapriya,[1,2] Devika Laishram,[1,3] Manoj K. Singh,[4] Rahul Singhal,[5] Sateesh Bandaru,[6,*] and Rakesh K. Sharma[1,7,*]

SUMMARY

Cubic spinel $LiMn_2O_4$ (LMO) are promising electrode materials for advanced technological devices owing to their rich electrochemical properties. Here, a series of Gd^{3+}-doped $LiMn_2O_4$ were synthesized using a simple one-step sol-gel synthesis, and a systematized study on the effect of increasing Gd^{3+} concentration on magnetic properties is conferred. The Raman and density functional theory (DFT) calculations of the synthesized materials were correlated with the magnetic properties; we observed a high coercivity value for the doped LMO compared to pristine LMO, which scales down from 0.57T to 0.14T with an increase in Gd concentration. The samples exhibited paramagnetic (at 300K) to antiferromagnetic (at 5K) transition and variation in the magnetic moment due to the replacement of Mn^{+2} or Mn^{+3} ion by Gd^{+3} ion from the octahedral 16d lattice site. The observed phase transitions in the hysteresis curve below the Neel temperature (T_N) at 5K are found to be due to the superexchange mechanism.

INTRODUCTION

Considering its unique crystal structure, lithium manganese oxides (LMO) are an excellent electrode material for various energy storage devices due to their rich electrochemical properties, thermal stability, and environmental friendliness.[1–4] Other than these, transition metal oxide and inorganic oxides are less used in the field of energy storage and other applications due to their structural, morphological, and optical property.[5–7] Commonly, LMO exhibits cubic spinel structure (ordered spinel) and belongs to the Fd3m space group in which Li, O, and Mn ion occupy the 8a tetrahedral (Td) sites, $32e^-$ position, and 16d octahedral (Oh) sites, respectively.[8–10] When this material is used as anode material in Li-ion batteries, severe capacity fading occurs due to the instability of Mn^{3+}, leading to dissolution in the electrolyte. Generally, Mn^{3+} and Mn^{4+} are distributed in 1:1 ratio; wherein more Mn^{3+} undergoes a strong Jahn-Teller (JT) distortion due to a single electron in Eg orbital.[11–13] To overcome this inhomogeneity, partial substitution of Mn^{3+} ions by electro-inactive rare earth elements was reported.[14] The dopant ion suppresses the JT distortion and stabilizes the spinel structure. Accordingly, doping of LMO by various transition metals[15,16] and rare earth metals[17,] and surface coating with metal oxides[18] were successively applied. The material exhibits exceptional structural, electrochemical, and magnetic properties.[19–21]

In addition to their electrochemical properties, $LiMn_2O_4$ and doped $LiMn_2O_4$ are fascinating material for studying the magnetic properties of geometrically frustrated spins because of the following intrinsic qualities: (i) Gadolinium-doped LMO showed expansion of LiO_4 tetrahedra and contraction of MnO_6 Oh unit resulting in replacement of geometrically frustrated spin state of $Mn^{3+}(t^3_{2g}e^1_g)$ and $Mn^{4+}(t^3_{2g}e^0_g)$ ion by Gd^{3+} ion, creating antiferromagnetic interaction.[22] (ii) Gd ions show multiple magnetic interactions with Mn^{3+}/Mn^{4+}, responsible for altered crystal structure and affecting the magnetic interaction. Mn-*O*-Mn geometry possibilities of LMO display paramagnetic, ferromagnetic, and antiferromagnetic transitions.[23] (iii) Mn^{3+} and Mn^{4+} are distributed into LMO lattice, wherein more Mn^{3+} ions undergo a strong JT distortion of a single electron in eg orbital ions, which can cause $Mn^{3+}O_6^{2-}$ Oh distortion. Magnetic measurements can investigate the magnetic structure and electrical properties of spinels used in lithium-ion battery technology.[24] Li ions have a nonmagnetic (diamagnetic) nature, which indirectly affects magnetic characteristics by influencing the cation valence of other lattice elements. The type of metal ions and electronic states determine the magnetic characteristics of the sublattice in the oxide framework. The magnetic properties can easily identify the minor variations that scanning electron microscopy (SEM), transmission electron microscopy (TEM), Fourier-transform infrared spectroscopy (FITR), and X-ray powder diffraction (XRD) cannot detect. Therefore, magnetism is also one of the essential tools

[1]Sustainable Materials and Catalysis Research Laboratory (SMCRL), Department of Chemistry, Indian Institute of Technology Jodhpur, Jodhpur, Rajasthan 342037, India

[2]Mechanical and Aerospace Engineering Department, College of Engineering, United Arab Emirate University, Al Ain 15551, UAE

[3]University College Dublin, School of Chemical and Bioprocess Engineering, Engineering Building, Belfield, Dublin 4, Ireland

[4]Centre of Material Sciences, University of Allahabad, Prayagraj 211002, India

[5]Department of Physics and Engineering Physics, Central Connecticut State University, New Britain, CT 06050, USA

[6]College of Materials and Environmental Engineering, Hangzhou Dianzi University, Hangzhou 310018, China

[7]Lead contact

*Correspondence: sbandaru@hdu.edu.cn (S.B.), rks@iitj.ac.in (R.K.S.)

https://doi.org/10.1016/j.isci.2022.105869

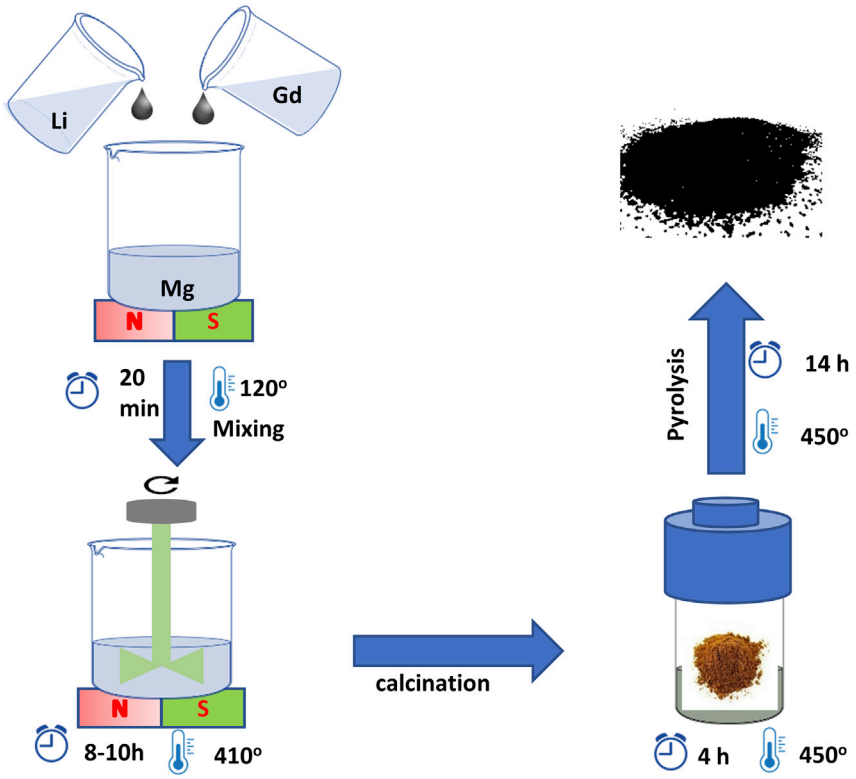

Scheme 1. The sol-gel synthesis procedure of $LiMn_{2-x}Gd_xO_4$

for material properties, which easily checks the quality of the materials. Apart from the energy storage applications, the Li-Mn-O family has piqued interest in magnetic interaction due to its orbital orientation changes at very low temperatures.[25–29] The contemporaneous charge order with structural transition and the complex magnetic characteristics of LMO at low temperature demonstrates the substantial interaction of charge, lattice, and magnetic degrees of freedom in $LiMn_2O_4$. The magnetic field of these doped LMO is controlled by factors like dopant metals particle size, morphology, distribution in spinel lattice, dispersion and synthesis pathway, etc.[30–32] A study on magnetic phase transitions of this material could give more insights into a deep understanding of material behavior toward electrochemical application. Herein, we report a low-temperature magnetic study of Gd^{3+} ion-doped LMO at 5K and 300K using zero-field-cooled (ZFC) and field-cooled (FC) techniques and the effect of 4f-3d interactions, transition, and rare earth metals. The effect of mass magnetization, saturation magnetization susceptibility, magnetic moment, and the site disorder with varied dopant concentrations are explored with the correlation of Raman and density functional theory (DFT).

RESULTS AND DISCUSSION

Structural and morphology analysis

As reported earlier, Gd doping in LMO was accomplished by a simple sol-gel route and is demonstrated in Scheme 1.[33] The phase purity and the crystal structure of pristine and doped samples of $LiMn_{2-x}Gd_xO_4$ (x = 0.00, 0.01, 0.02, 0.03, and 0.04) were analyzed by XRD in Figure 1. The sharp, intense peaks confirmed the formation of highly crystalline cubic spinel LMO in accordance with Joint Committee on Powder Diffraction Standards (JCPDS) No. 35–0782. The doped materials showed peaks of lower intensity between 2θ from 28° to 33° and 73° to 77° due to the formation of $GdMn_2O_5$ during the oxidation in the presence of partial pressure of oxygen.[34] Moreover, the low-intensity peaks denote the maximum incorporation of Gd into the spinel lattice.[34] Upon increasing Gd doping, the high intense XRD peak of pristine LMO is shifted to higher 2θ (inset Figure 1) due to higher ionic radii of Gd^{3+} ion, which further confirms the substitution of Gd ion in place of Mn.[36] Morphological variation in LMO upon Gd doping was observed in the TEM images (Figures 2A–2F). In Figure 2D, Gd04 exhibits minute granular structures due to high Gd doping compared to pristine LMO. The fast Fourier transform (FFT) images Figures 2C and 2F and the d-spacing (0.47 nm) were calculated from the High-resolution transmission electron microscopy (HRTEM) images,

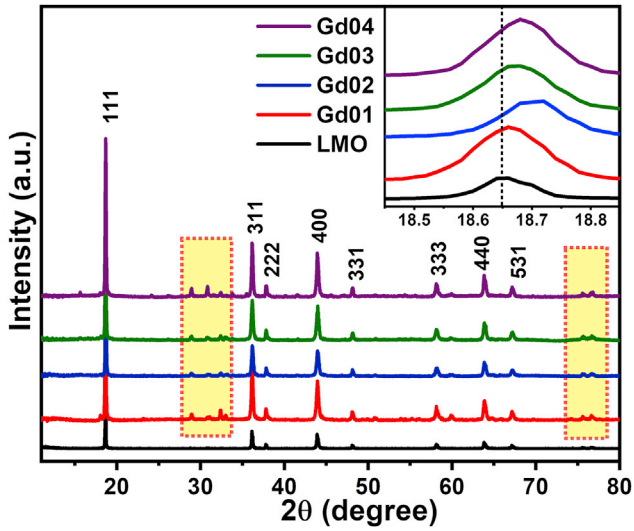

Figure 1. XRD patterns for $LiMn_{2-x}Gd_xO_4$ samples and inset enlarge view of (111) plane

which correspond to the highest intense XRD plane (111), as seen in Figure 1. The high thermal stability of Gd-doped LMO from room temperature to 650°C is observed from TGA graphs as shown in Figure S1, where Gd02 exhibited exceptional stability and minimum weight loss of 0.4% compared to Gd01 (1.6%).

Figure 3 discloses the surface morphological features of all Gd LMO samples via SEM. Minor variations in the size and Oh morphology were observed on doping. Figure 3A represents the SEM images of pristine LMO crystals, revealing the truncated Oh morphological features with both size and shape inhomogeneity. Figures 3B–3E depicts the SEM images of Gd LMO samples, and it is evident that doping does not affect any morphological variations. The average crystal size was found to be around 1 μm for pristine LMO, which upon doping, resulted in a decrease in the particle size (0.5–0.8 μm). Figures 3F and 3G are the corresponding Energy Dispersive X-Ray Analysis (EDX) spectrum for pristine LMO and Gd01 samples, which confirm the presence of Mn, O, and Gd. In addition, EDX mapping of Gd01 and Gd02 shows the distribution of the atoms, which confirms the homogeneous doping of Gd into LMO spinels, as shown in Figure S2. The attachment of different functional groups in the synthesized materials was analyzed using FTIR studies; corresponding spectra are given in Figure S3. The obtained FTIR spectrum of LMO shows absorption bands at 862 and 1089 cm^{-1}, respectively, corresponding to the metal-oxygen (Mn-O) vibrational frequencies. The low-frequency broadbands are associated with -OH peaks, indicating less crystalline water in the LMO lattice. The surface compositions of the prepared materials are analyzed by using the X-ray photoelectron spectroscopy (XPS) technique. The XPS survey scan of LMO and Gd LMO is given in Figure 4A, which confirms the presence of Mn, O, Li, and Gd. The binding energy for Li 1s at 53.87 eV may be due to Li^+ ion as shown in Figures 4B and 4F. The Mn2p spectral peaks were clearly separated into the two oxidation states of $Mn2p_{3/2}$ and $Mn2p_{1/2}$, by about 11.5 eV. These binding energies are quite similar to the previous report. In Mn 2p spectrum, the two peaks of each Mn $2P_{3/2}$ and Mn $2P_{1/2}$ are separated into two valance states of Mn^{3+} and Mn^{4+}. Figure 4C shows the binding energies of Mn^{3+} are deconvoluted at 641.82 eV (Mn $2p_{3/2}$) and 653.58 eV (Mn $2p_{1/2}$), whereas Mn^{4+} shows deconvoluted peaks at 645.32 eV (Mn $2p_{3/2}$) and 657.54 eV (Mn $2p_{1/2}$).[36,37] Figure 4G indicates the binding energies of Gd-doped LMO for Mn^{3+} at 641.58 (Mn $2p_{3/2}$) and 653.26 (Mn $2p_{1/2}$) and for Mn^{4+} at 645.02 (Mn $2p_{3/2}$) and 657.34 (Mn $2p_{1/2}$).[35,38] Variation in the peaks of Mn^{3+} and Mn^{4+} can be attributed to the Gd interaction with the Mn ion. Gd 4d core level shows three peaks at 141.12 eV, 146.34 eV, and 153.14 eV assigned to the Gd metal peak ($LiMn_{1.95}Gd_{0.5}O_4$), Gd-Ox, and Gd satellite peak, respectively, as shown in Figure 4E.[36] The oxide form supports the presence of Gd(III) species.[37] The deconvoluted O 1s spectrum displayed in Figure 4C indicates two peaks at 529.7 and 531.4 eV owing to the surface oxygen present in Mn or Gd Oh sites and Li Td sites, respectively.[39,40]

Raman analysis

Raman spectroscopy was used to investigate the structural changes in Gd-modified $LiMn_2O_4$ samples. Based on group theory, the cubic structure of $LiMn_2O_4$ with space group Fd3m (Oh7) yields

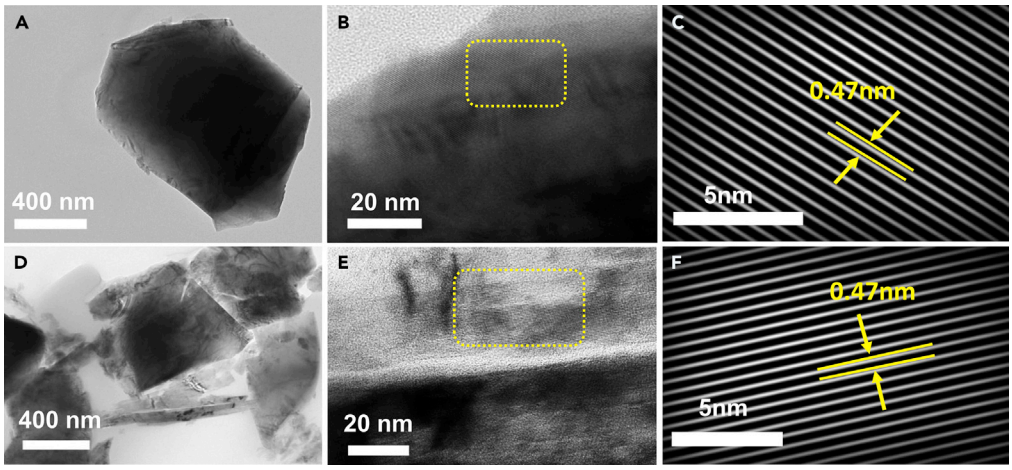

Figure 2. Low- and high-magnification TEM images of (A and B) pristine LMO and (D and E) GD04
(C and F) inversed fast Fourier transform (IFFT) of as-prepared catalyst of pristine LMO and Gd04, respectively.

(*Raman, = A_g + E_g + $3F_{2g}$) active Raman modes.[41] Figure 5A shows the Raman spectra of Gd-modified LMO samples measured at room temperature. In order to prevent thermal decomposition, a laser power of 10 mW was used. The second phase of composite materials is $GdMn_2O_5$, which is a paramagnetic material with an orthorhombic structure at room temperature. The group theory analysis predicted that the orthorhombic phase would have a *Pbam* space group and would yield 48 Raman active modes (*Raman, R3c = 13Ag+13B1g+11B1g+11B1g).[42] Owing to Gd substitution at the Mn^{3+} and Mn^{4+} sites, there is dispersion within the bond lengths of the modified $LiMn_2O_4$ samples. This produces subtle changes in electron distributions. Thus, only a few main higher Raman modes (>500 cm^{-1}) are clearly distinguishable. In Figure 5B, the Raman spectrum of $LiMn_2O_4$ shows a broad and dominant Raman band at approximately 630 cm^{-1} and a shoulder at approximately 600 cm^{-1}, both assigned as A_{1g} and F_{2g} modes, respectively. Raman vibrations at 630 cm^{-1} correspond to symmetric stretching vibrations of Mn-O groups in MnO_6. Among the factors affecting the widening of 630 cm^{-1} are bond lengths of the cations and anions, as well as the degree of polyhedral distortion produced by LMO, which consists of distorted Oh (Mn^{3+} O_6) due to the JT effect and isotropic Mn^{4+} O_6. Raman mode near ~600 cm^{-1}, the shoulder peak, is mainly caused by the Mn^{4+}-O bonding and is very sensitive to lithium ions in LMO. These two Raman modes are responsible for regulating the magnetic phase and spinefl phase of LMO samples. Nevertheless, low-wavenumber Raman modes are observed and assigned as ~510 (F_{2g}), ~452 (Eg), and ~382 (Eg) and mainly originate from Li-O stretching bonds, O-Li-O, O-Mn^{3+}-O, and O-Mn^{4+}-O bending vibrations. These modes are very weak in intensity compared to Ag mode at 600 cm^{-1}. In this case, we are able to detect Raman modes with cubic symmetry-based $LiMn_2O_4$ samples based on differentiating the sample from the second phase orthorhombic $GdMn_2O_5$. However, it is not feasible to determine the exact frequency of Raman modes. Furthermore, Gd^{3+} ion doping itself creates disorder at the atomic level, which results in a diffuse spectrum. For this reason, it is difficult to accurately identify and assign mode frequencies. Raman modes of polycrystalline complex two-phase structures of Gd-doped LMO samples are difficult to identify. A similar explanation can be found in the literature.[43] When Mn^{3+}/Mn^{4+} ions are partially substituted by Gd^{3+} ions, they cause Mn-site disorders in LMO, resulting in anomalous shifting of Raman modes toward higher frequencies (blue shift), and the rapid absence of certain modes, as shown by X-ray diffraction. In addition, components such as the binding strength force constant and change in effective mass can affect Raman mode shifting. As the atomic masses of Mn^{3+}/Mn^{4+} ions were replaced by Gd^{3+} ions in the LMO lattice, an anomalous change in Raman modes was observed since Gd^{3+} (157.9 g) has a higher atomic mass than Mn (54.0 g). This leads to an increase in effective mass and force constant of Gd^{3+}-modified LMO lattice and Mn^{3+}-O and Mn^{4+}-O stretching bond distortion. LMO compounds doped with Ce, Gd, and Nd were also reported to have similar properties.[43,44] Raman modes of low intensity in LMO are shifted and transmitted as broad peaks as a result of Gd doping. As Gd concentration increases, Raman modes with higher frequency modes become more prominent, possibly due to increased orthorhombic phase in Gd04 sample. Sample (Gd04) shows additional new Raman modes near 212 cm^{-1} and 678 cm^{-1} (* in Figure 5A), indicating the presence of $GdMn_2O_5$. The results also support XRD of Gd-doped $LiMn_2O_4$ samples.

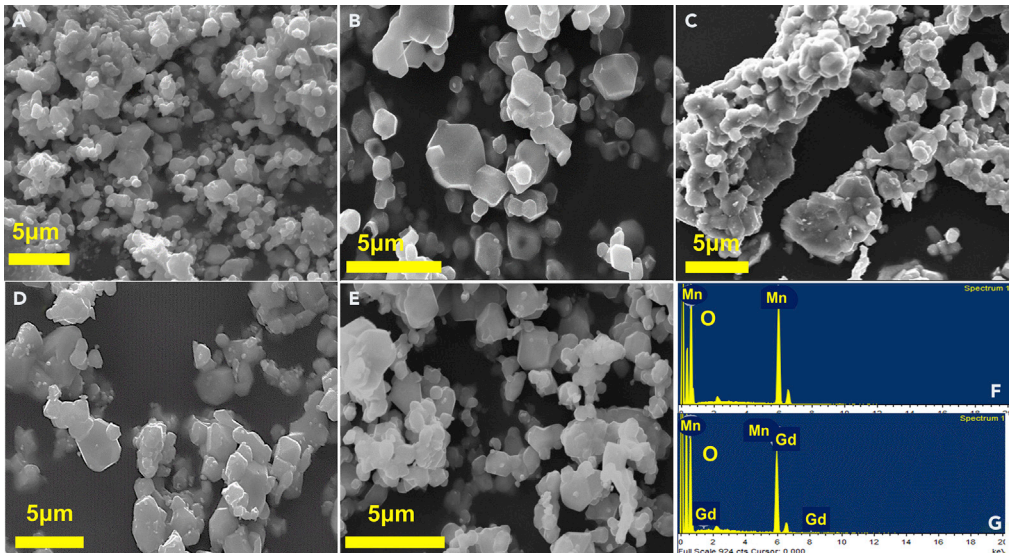

Figure 3. SEM image of pristine LMO (A) and Gd-doped LMO with different concentrations (A–E) and EDX mapping of LMO and Gd04 (F and G)

First-principles calculations

In order to further understand and elucidate the electronic, magnetic, and structural changes of Gd-doped materials, first-principle calculations were carried out on lattice models of $LiMn_2O_4$ and doped $LiMn_{2-x}Gd_xO_4$ systems. The $LiMn_2O_4$ belongs to the space group Fd3m and the corresponding fully relaxed structure as shown in Figure 6. $LiMn_2O_4$ has cubic close-packing arrangement and contains 8 Li's, 16 Mn's, and 32 O's ions in a cell, and the corresponding molecular formula is $Li_8Mn_{16}O_{32}$. The DFT + U computed lattice parameters of $LiMn_2O_4$ is a = 8.358 Å, which is slightly higher than that of the standard value (8.321 Å), and Mn-O distance is 1.995 Å, slightly elongated compared to the standard value (1.934 Å); both these parameters are in excellent correlation with the experimental value. Doping formation energies were calculated using the following formula: Gd-substitution in $LiMn_2O_4$

The substitution energy of Gd in $Li_8Mn_{16-x}Gd_xO_{32}$, i.e., the change in the formation energy of Gd-substituted $Li_8Mn_{16-x}Gd_xO_{32}$ with respect to $Li_8Mn_{16}O_{32}$ is

$$E_{sub} = E_{Li8Mn16-xGdxO32} - E_{Li8Mn16O32} - x\mu_{Gd} + x\mu_{Mn} \quad \text{(Equation 1)}$$

where, $Li_8Mn_{16-x}Gd_xO_{32}$ and $Li_8Mn_{16}O_{32}$ are total energies of Gd-doped $Li_8Mn_{16-x}Gd_xO_{32}$ systems and pure $LiMn_2O_4$ supercell, and $x\mu_{Gd}$ and $x\mu_{Mn}$ are chemical potentials of Gd and Mn atoms.

Fully relaxed LMO results in the mono-doping, double-doping, and up to the penta-doping case with the DFT data are listed in Table 1, and all fully c/a relaxed pure and Gd-doped structures are shown in Figure 6. For the Gd-doped system, it is understood that the lattice constants and volumes are increased with increasing Gd-doping concentration; a possible reason might be that the ionic radius of Gd^{3+}(0.938 Å) is higher than that of $Fe^{2+/3+}$ (0.76 Å/0.645 Å). The formation energies of the Gd-doped $Li_8Mn_{16}O_{32}$ supercell have been shown in Table 1. The formation energies of Gd-doped structures ($Li_8Mn_{16-x}Gd_xO_{32}$ supercell) are negative values, indicating that the doping process is energetically more favorable and experimentally more promising while increasing the Gd-doping concentration, and it further stabilizes the Gd-doped systems. To explore the magnetic behaviors of Gd-doped $Li_8Mn_{16}O_{32}$ supercell, DFT + U calculations have been performed. The computed magnetic momentum for the Mn in $Li_8Mn_{16}O_{32}$ supercell is 3.82 μ_B, consistent with earlier studies.[45] In general, Gd will contribute 7 μB magnetic moment; thus, Gd doping enhances the magnetism of $Li_8Mn_{16-x}Gd_xO_{32}$ (x = 1–5) doped systems. The computed atomic magnetic moments of *mono-, bis-, tri-, tetra- and penta*-Gd atom doped in $Li_8Mn_{16}O_{32}$ supercell are provided in Table 1. From Table 1, an enhanced magnetic momentum is observed while increasing the Gd-doping concentration in $Li_8Mn_{16}O_{32}$ supercell, which states that more dopant (Gd) incorporation in $Li_8Mn_{16}O_{32}$ should result in more magnetic momentum. The atomic magnetic momentum of the Gd doped in $Li_8Mn_{16}O_{32}$ systems was enhanced and observed up to 0.08 Gd-doping

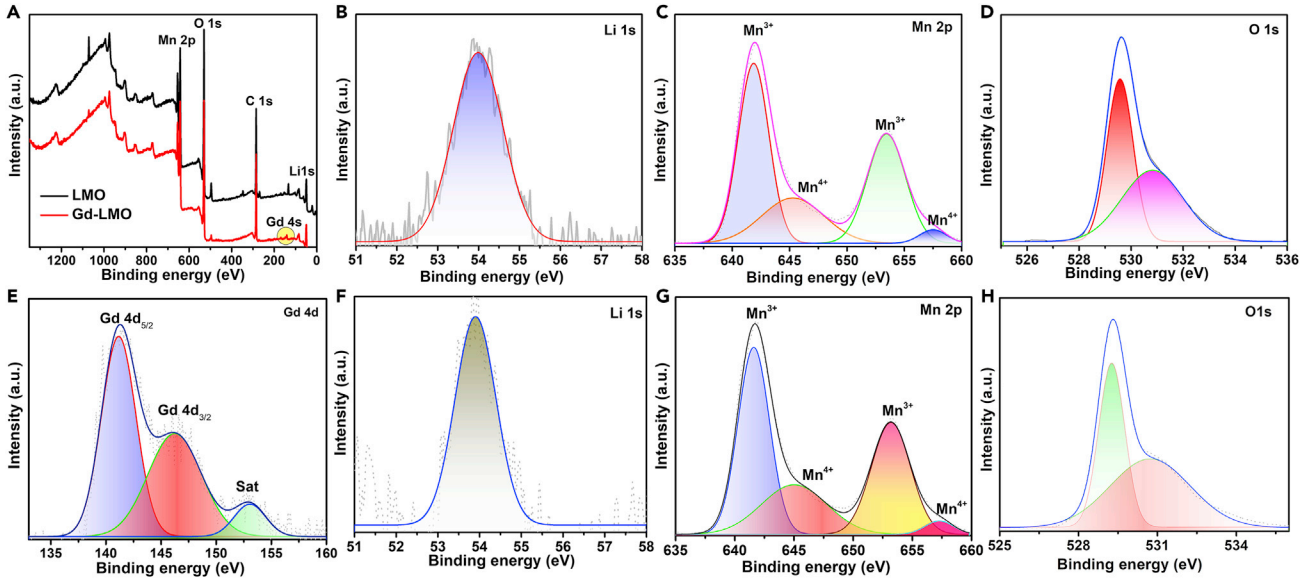

Figure 4. XPS spectra of as-prepared materials: (A) survey spectra of LMO and Gd-LMO

(B) High-resolution spectra of LMO (B–D) and Gd-LMO (E–H).

concentration. It is also observed that these doped systems' atomic spin magnetic momentum is decreased above 0.08 Gd-doping concentration, which is well matched with the experimental observation. At high Gd-doping concentrations, exchange interactions and redistribution of the charge will occur, and the magnetic properties of these $Li_8Mn_{16}O_{32}$ systems depend on the Mn^{3+}-Mn^{3+} interaction with *3d-4f* election spin coupling. At low concentrations, the Gd^{3+} atoms enter the Mn^{3+} lattice, and Gd^{3+}-Mn^{3+} interaction occurs through the *3d-4f* election coupling (Figure 6A). The partial density of states of $Li_8Mn_{15.96}Gd_{0.04}O_4$ and $Li_8Mn_{15.81}Gd_{0.19}O_4$ has been shown in Figure 7. From projected density of states (PDOS) of $Li_8Mn_{15.96}Gd_{0.04}O_4$, coupling is possible *3d* of Mn^{3+} (red line) and *4f* of Gd^{3+} atoms (green line). At high Gd-doping concentrations ($Gd_{0.19}$) *3d-4f* election coupling would be stronger than (Figure 7B) Gd-doping at low concentration (0.04). Thus, slight reductions in magnetic momentum values of Mn^{3+} (3.282 μ_B) and Gd^{3+} (7.117 μ_B) are observed in the $LiMn_{15.81}Gd_{0.19}O_4$ doped system.

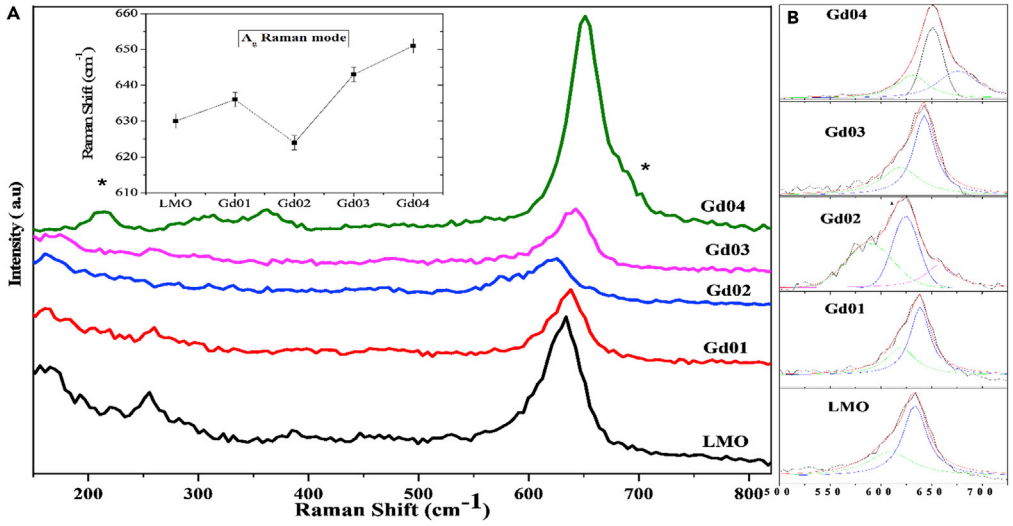

Figure 5. (A) Raman spectra of the Gd-doped $LiMn_2O_4$ samples at room temperature in the frequency range from 150 to 800 cm^{-1}

Anomalous frequency shift in Ag Raman mode in Gd-doped LMO samples is shown in the inset.

(B) Lorentzian fit of Ag and F2g modes in $LiMn_2O_4$ samples doped with Gd.

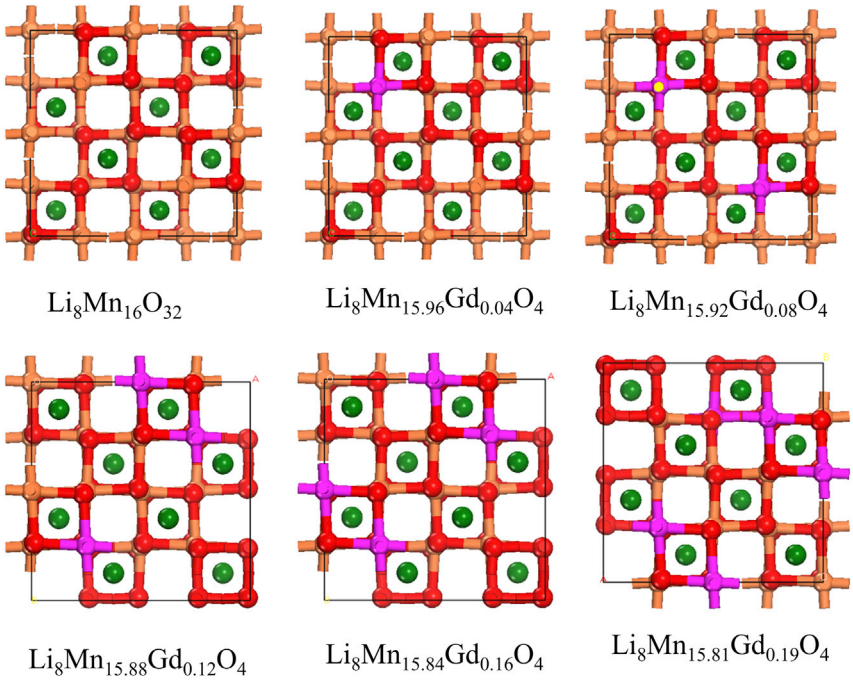

Figure 6. Fully relaxed structures of pure $LiMn_{16}O_{32}$ and Gd-doped $Li_8Mn_{16-x}Gd_xO_{32}$ (x = 0.04 to 0.19) supercell systems (top view)

Magnetic properties

Magnetization characteristics are subjected to various extrinsic and intrinsic factors such as dopant grain size, atomic composition, density, anisotropy, bond length, bond angle, and cation distribution between Gd^{3+} and Mn^{3+}or Mn^{4+}.[46] Gd ions show multiple magnetic interactions with Mn^{3+}/Mn^{4+}, which are responsible for altered crystal structure and affect the magnetic interaction. Possible magnetic interaction is (1) Mn^{3+}-O-Mn^{4+}, (2) Mn^{3+}- O-Mn^{3+}, (3) Mn^{4+}-O-Mn^{4+}, (4) Gd^{3+}-O-Mn^{4+}, (5) Gd^{3+}-O-Mn^{3+}, and (6) Gd^{3+}-O-Gd^{3+} in which ferromagnetism is showing at low temperature due to (4), (5), and (6) type of interaction. Temperature-dependent magnetization of all samples was recorded by ZFC and FC mode under an external magnetic field of 200 Oe from 300K to 5K, (Figures 8A–8D). When the temperature drops below 70 K, the temperature-dependent behavior of the ZFC and FC curves is observed to be qualitatively different for different applied magnetic field strengths. Both ZFC and FC highlight paramagnetic, diamagnetic, ferromagnetic or antiferromagnetic, and exchange coupling of lattice ions.[47] During cooling, particles tend to magnetize to minimize the magneto-crystalline energy. Blocking temperature (T_B) is the temperature at which the magnetic anisotropy energy barrier is overcome by thermal activation, leading to the fluctuation of its magnetization. The value

Table 1. Lattice constant *a* (in Å), atomic volumes (Å^3), magnetic moment (in μB), bond distances, formation energies (in eV)

System	Lattice parameters	Volume/ion (in Å^3)	μ_B	ΔE_{form}
$Li_8Mn_{16}O_{32}$	8.358	10.42	3.817	
$LiMn_{15.96}Gd_{0.04}O_4$	8.426	10.68	7.132	−4.63
$LiMn_{15.92}Gd_{0.08}O_4$	a = 8.597 c = 8.309	10.95	7.133	−7.74
$LiMn_{15.88}Gd_{0.12}O_4$	a = 8.651 c = 8.403	11.22	7.131	−11.13
$LiMn_{15.84}Gd_{0.16}O_4$	a = 8.75 c = 8.462	11.57	7.126	−13.08
$LiMn_{15.81}Gd_{0.19}O_4$	a = 8.802 c = 8.570	11.57	7.117	−16.97

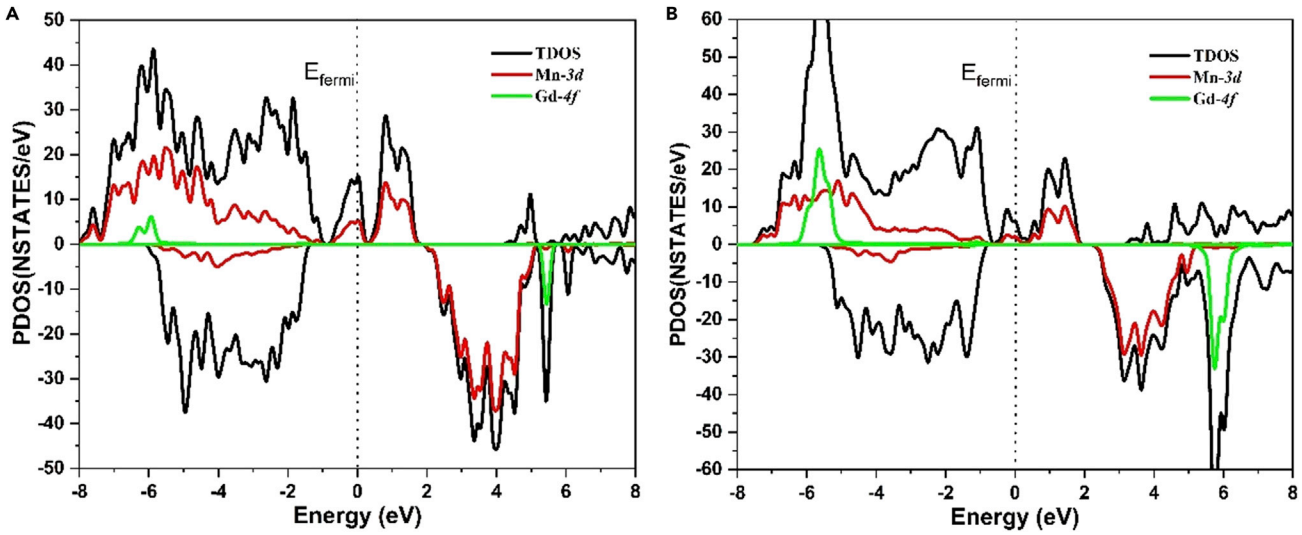

Figure 7. Total densities of states and PDOS were computed for the $Li_8Mn_{15.96}Gd_{0.04}O_4$ (A) and $Li_8Mn_{15.81}Gd_{0.19}O_4$ (B) using DFT + U

of T_B is almost equal to pristine LMO, except Gd01. T_B is not dependent on the doped Gd concentrations but mainly upon the interactions between the atoms. From T_B to lower-temperature region, the system moves toward either ferro- or antiferromagnetic. Above T_B, thermal vibration becomes stronger over the Zeeman interaction due to more thermal energy, causing randomization of the magnetic moment orientation and decreasing the magnetization value. The obtained T_B values for LMO, Gd01, Gd02, Gd03, and Gd04 systems are 46.49, 41.71, 46.70, 47.25, and 47.30 K, respectively. In the case of Gd01, there will be more Mn - Mn interaction to reduce the antiferromagnetic interactions. The decrease in T_B temperature for Gd01 can be explained on the basis of the interaction between the doped and the lattice ion. The inverse susceptibility of all the Gd-doped LMO was plotted and shown in Figures 9A–9D. Figure 9A shows the chance of more than one phase transition present in the lattice responsible for the sudden decrease in T_B value and Mn - Mn interaction and started paramagnetic to antiferromagnetic transformation at a very high temperature. Furthermore, the Neel temperature (T_N) of the Gd03 compositions (Figure 9C) indicated the highest value compared to other compositions. The extracted Curie-Weiss parameters for Gd01 are θc = −271.48 K and Cp = 4.77 emu K/mol from the linear fit of the inverse susceptibility. The other estimated Curie temperatures are −297.73, −289.47, and −198.21 K for Gd02, Gd03, and Gd04, respectively, indicating paramagnetic behavior above 70 K. The negative Weiss constant indicates that the Antiferromagnetic (AFM) interactions get stronger as the proportion of Mn^{3+} rises, owing to the increased number of AFM rough involving Mn^{3+}.[48] It can be concluded that those antiferromagnetic interactions of the Mn^{3+} ion spins are dominant over ferromagnetic superexchange interactions. The effective magnetic moment of LMO (6.1 μ_B mol^{-1}) obtained from inverse susceptibility (Figure S4) indicates a valence state of $Mn^{3+/4+}$, apparently in 3:1, which can be easily seen in the XPS plot. According to previously reported results, it can be noted that an effective magnetic moment corresponds to a high spin state of Mn^{3+} in the LMO lattice.[25] These are the exchange interaction components across a shared Oh-site edge in $LiMn_2O_4$. The Curie-Weiss parameter for other Gd-doped LMO are given in Table 2. It is clearly observed that effective magnetic moment increases with the Gd doping and further decreases up to 6.35 μB, and the same trend was observed in DFT studies. At low concentrations, the Gd^{+3} atoms enter into the Mn^{3+} lattice and Gd^{3+}-Mn^{3+} interaction occurs through the *3d-4f* election coupling (Figure 6A). At high Gd-doping concentrations, exchange interactions and redistribution of the charge will occur, and the magnetic properties of these $Li_8Mn_{16}O_{32}$ systems depend on the Mn^{3+}-Mn^{3+} interaction with *3d-4f* election spin coupling. At high Gd-doping concentrations ($Gd_{0.19}$) *3d-4f* election coupling would be stronger than the (Figure 6B) Gd-doping at low concentrations.

In addition, isothermal magnetic hysteresis analyses were measured from +5 to −5 T at 300 k (Figures 10A–10D). At low temperatures (5 K), the sigmoidal shape curve suggests magnetic phase transfer from paramagnetic to magnetically ordered antiferromagnetic.[49] The computed magnetic moments of Mn^{4+}, Mn^{3+}, and Gd^{3+} are 3.03–3.40, 3.88–4.00, and 7.11 μ_B, respectively.[50] The magnetic dipolar orientation of the rare earth exhibits a disordering form at room temperature. As a result, it's possible that rare earth ions (Gd^{3+}) are

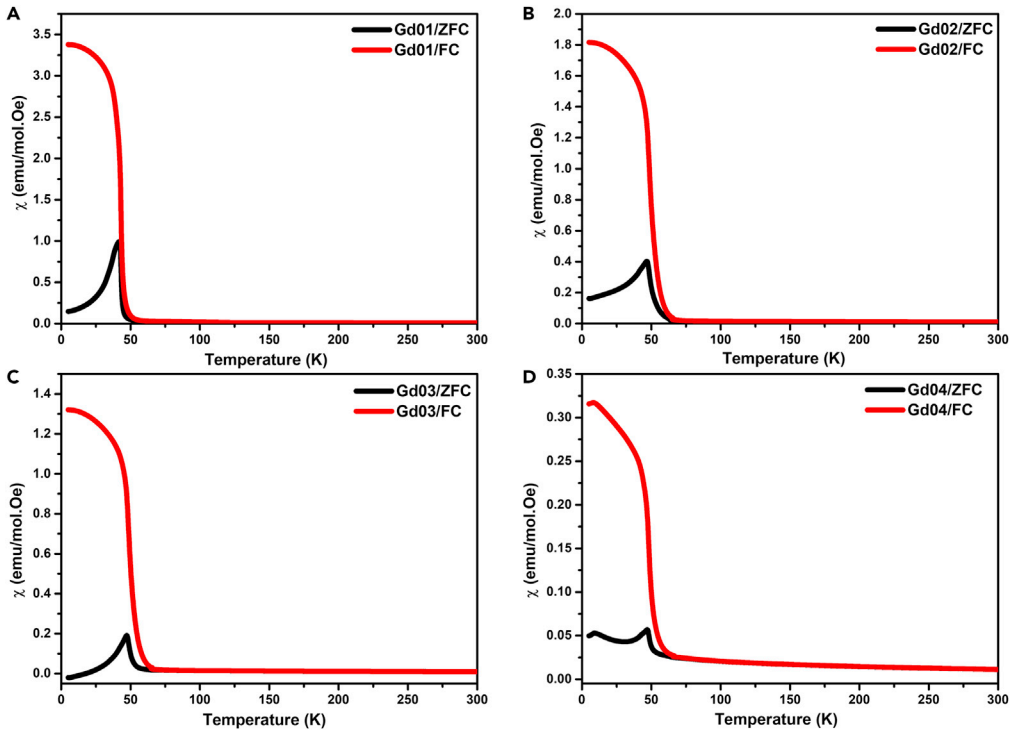

Figure 8. ZFC and FC magnetization under magnetic field of 200 Oe for (A) Gd01 (B) Gd02, (C) Gd03 and (D) Gd04 from 5k to 300k

nonmagnetic at room temperature, which can be easily seen in M-H plots.[51] This enhancement in the magnetic properties is attributed to the higher magnetic moment of Gd doping in LMO enhancing the magnetic properties of materials owing to the higher moment of Gd^{3+} ($4f^7$) which is located in the Oh 16d lattice site. Higher concentrations of Gd^{3+} lead to a decrease in the coercivity of LMO spinel as more energy is required for magnetization or demagnetization. The coercivity measures the magneto-crystalline anisotropy of Gd LMO, which depends upon engaged vacancies of Mn ion at the Oh sites, concentration, and ionic radii of the Gd dopant.[52] The coercivity is influenced by factors like morphology, grain size, porosity, domain structure anisotropy, and ion exchange. As a result of the orientation of cation distribution between Gd^{3+} and Mn^{2+} or Mn^{3+} (strong Gd-Mn superexchange interaction) in the spinel system, Li ions have no magnetic interaction with the other lattice ions, but Mn and Gd have interaction at the 8a Td and 16d Oh sites. The geometry of cubic spinel has interatomic 3d metal and 4f metal interaction at the 16d Oh site through the weak overlapping between the Mn ion with Gd ion(t_{2g}-4f) and Mn-O with Gd ions (t_{2g}-*O*-4f). High-spin Gd^{3+} ion holds three unpaired electrons in T_1u, while Mn^{3+} and Mn^{4+} have one unpaired and three electrons, in which the last electrons are in Eg and t_{2g} orbital, respectively. According to Goodenough, the interaction between Mn^{4+} has antiferromagnetic interaction due to the direct overlapping of t_{2g}-t_{2g}.[53] Gd01 has the highest coercivity of 0.58 T and remanent magnetization of 4.9 over all the other synthesized materials, which might be due to an early starting of antiferromagnetic interaction through the T_1u-$2p_{\pi\sigma}$-t_{2g}/Eg interaction that dominates over other ferromagnetic and paramagnetic interaction.[54] Coercivity, remanent magnetization, and Curie-Weiss fit obtained for the doped materials are shown in Table 2. This increase in magnetization is attributed to higher unpaired electron of Gd^{3+} ($4f^7$) compared to $Mn^{3/4+}$ ion placed at 16d Oh sites and may also be due to released Mn ion from Oh, rearranging in antiparallel manner.[55] Gd02 shows the highest magnetic moment among the doped materials (Hc = 0.56 T and Mr of 2.31 emu g^{-1}) which is possibly due to the combined effect of Mn^{3+}-Mn^{3+} interaction with 3d-4f election spin coupling.

Conclusion

The Gd-doped LMO was successfully prepared by a one-pot hydrothermal sol-gel route. A detailed analysis of magnetic susceptibility, inverse susceptibility, coercivity-remanent magnetization, and magnetic moment was studied by correlating with Raman and DFT analysis. The obtained results observed a high coercivity value for the doped LMO compared to pristine LMO, which scales down from 0.57 T to 0.14 T with an increase in Gd

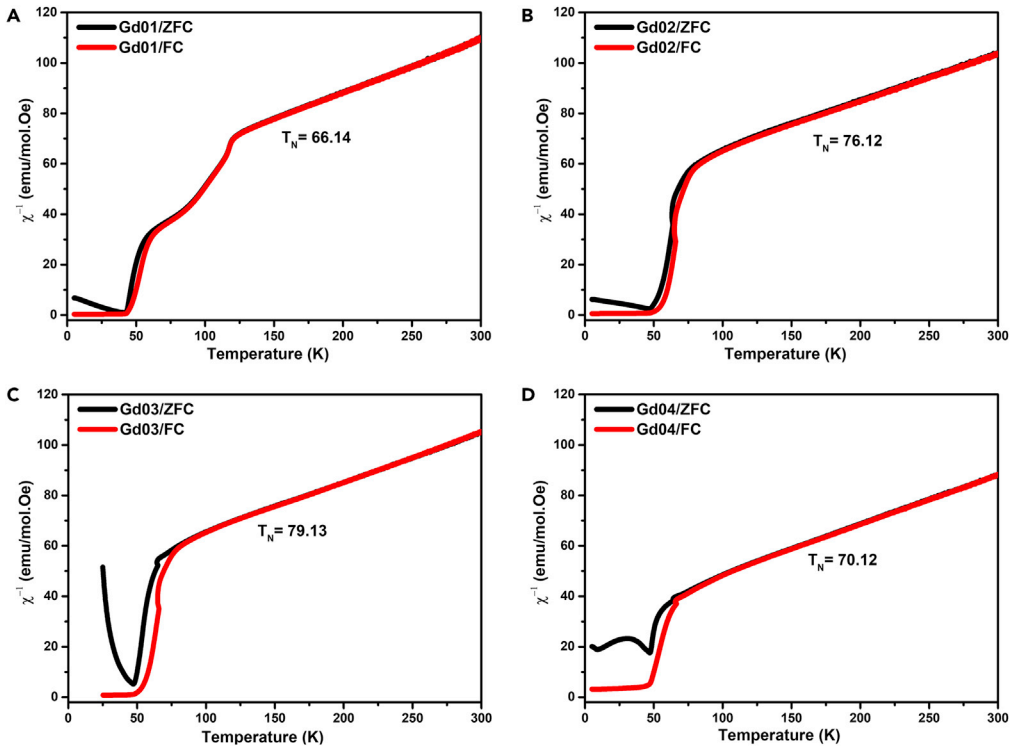

Figure 9. χ-1Vs T plot under magnetic field 200 Oe for (A) Gd01 (B) Gd02, (C) Gd03 and (D) Gd04 from 5k to 300k

concentration. The current study revealed that Gd LMO shows paramagnetic nature at room temperature and undergoes paramagnetic to antiferromagnetic phase transition at very low temperatures owing to ion exchange between Mn and Gd ion. The susceptibility follows the Curie-Weiss law with a negative Weiss constant indicating the dominated antiferromagnetic interaction over paramagnetic. The obtained magnetic moment of the materials is due to the combined effect of Mn^{3+}-Mn^{3+} interaction with *3*d-4f election spin coupling. Gd02 showed the highest magnetic moment (6.50μ_B) with Mr of 2.31 emu g^{-1} and Hc of 0.56 T.

Limitation of the study

The cost of the synthesized materials via doping of rare earth could become one of the major challenges with this approach. It is, therefore, important to synthesize materials based on earth-abundant metals, which can be tested for energy materials. In this study, the magnetic properties of the energy storage catalyst (Gd-doped LMO) correlated only with the Raman spectroscopy and DFT calculations but did not correlate with the electrochemical properties. This requires further studies to understand the relationship between electrochemical properties and magnetic behaviors.

STAR★METHODS

Detailed methods are provided in the online version of this paper and include the following:

- KEY RESOURCES TABLE
- RESOURCE AVAILABILITY

Table 2. Magnetic parameter of $LiMn_{2-x}Gd_xO_4$ samples

Sample	Composition	Mr (emu g^{-1})	H_C(Tesla)	Θ_c(Temp.)	μ_{eff} (μ_B)
Gd01	$LiMn_{1.99}Gd_{0.01}O_4$	4.902	0.576	−271.48	6.17
Gd02	$LiMn_{1.98}Gd_{0.02}O_4$	2.31	0.567	−297.73	6.50
Gd03	$LiMn_{1.97}Gd_{0.03}O_4$	0.593	0.215	−289.47	6.40
Gd04	$LiMn_{1.96}Gd_{0.04}O_4$	0.47	0.146	−198.21	6.35

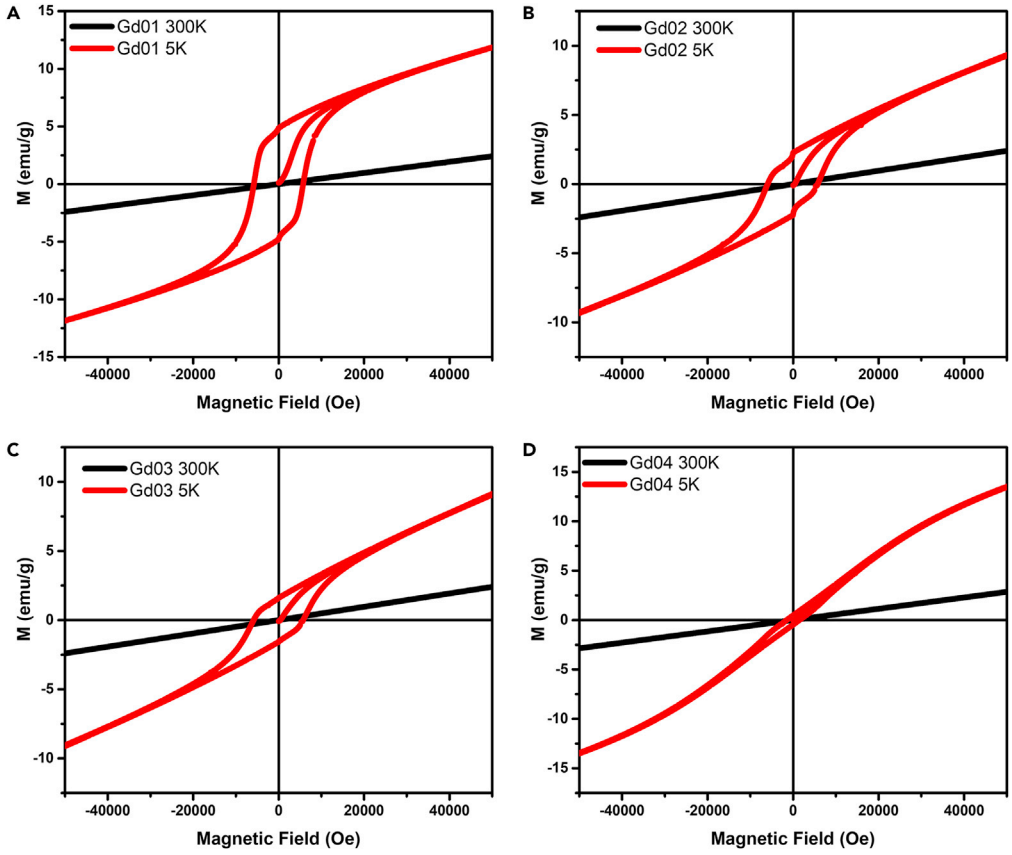

Figure 10. Magnetization of all the Gd-doped LMO (A) Gd01 (B) Gd02, (C) Gd03 and (D) Gd04 at room and 5K temperature with applied field of ± 5T

SUPPLEMENTAL INFORMATION

Supplemental information can be found online at https://doi.org/10.1016/j.isci.2022.105869.

ACKNOWLEDGMENTS

The authors thank Ministry of Education for financial support. We also thank Center for Advanced Scientific Equipment (CASE)-IITJ and Scientium Analyze Solutions for characterizations. Authors are grateful for financial support to SERB-CRG-India (grant number CRG/2020/002163) and DBT PAN IIT Center for Bio-energy (grant number BT/PR41982/PBD/26/822/2021).

AUTHOR CONTRIBUTIONS

B.S.: Methodology, Conceptualization, Experimental Investigations, Formal Analysis, Writing-Original draft, Writing- Review & Editing, R.K, D.L., R.K.S, and R.S.; are involved in the conceptualization of research ideas, formal analysis, Writing-Review & Editing, M.K.S; analyzed and writing the Raman data, Y.J; DFT

analysis and drafted the DFT analysis. R.K.S was involved in funding acquisition and supervision of the entire work.

DECLARATION OF INTERESTS

The authors declare no competing interests.

Received: October 28, 2022
Revised: November 28, 2022
Accepted: December 21, 2022
Published: January 20, 2023

REFERENCES

1. Goodenough, J.B. (2007). Cathode materials: a personal perspective. J. Power Sources *174*, 996–1000. https://doi.org/10.1016/j.jpowsour.2007.06.217.

2. Pulido, R., Naveas, N., JMartín-Palma, R., Graber, T., Brito, I., Hernández-Montelongo, J., and Manso Silván, M. (2022). Experimental and density functional theory study of the Li+ desorption in spinel/layered lithium manganese oxide nanocomposites using HCl. Chem. Eng. J. *441*, 136019. https://doi.org/10.1016/j.cej.2022.136019.

3. Thackeray, M.M., David, W.I.F., Bruce, P.G., and Goodenough, J.B. (1983). Lithium insertion into manganese spinels. Mater. Res. Bull. *18*, 461–472. https://doi.org/10.1016/0025-5408(83)90138-1.

4. Huang, Y., Dong, Y., Li, S., Lee, J., Wang, C., Zhu, Z., Xue, W., Li, Y., and Li, J. (2021). Lithium manganese spinel cathodes for lithium-ion batteries. Adv. Energy Mater. *11*, 2000997. https://doi.org/10.1002/aenm.202000997.

5. Magesh, G., Bhoopathi, G., Nithya, N., Arun, A.P., and Ranjith Kumar, E. (2018). Structural, morphological, optical and biological properties of pure ZnO and agar/zinc oxide nanocomposites. Int. J. Biol. Macromol. *117*, 959–966. https://doi.org/10.1016/j.ijbiomac.2018.04.197.

6. Indumathi, T., Theivarasu, C., Pradeep, I., Rani, M.T., Magesh, G., Rahale, C.S., and Kumar, E.R. (2021). Effects of Nd doping on structural, optical, morphological and surface-chemical state analysis of ZnO nanoparticles for antimicrobial and anticancer activities. Surface. Interfac. *23*, 101000. https://doi.org/10.1016/j.surfin.2021.101000.

7. Ranjithkumar, B., Ranjith Kumar, E., Srinivas, M., Ramalingam, H.B., Srinivas, C., Magesh, G., Balamurugan, A., Rahale, C.S., and ChandarShekar, B. (2021). Evaluation of structural, surface morphological and thermal properties of Ag-doped ZnO nanoparticles for antimicrobial activities. Phys. E Low-dimens. Syst. Nanostruct. *133*, 114801. https://doi.org/10.1016/j.physe.2021.114801.

8. Hosoya, M., Ikuta, H., Uchida, T., and Wakihara, M. (1997). The defect structure model in nonstoichiometric LiMn2 O 4 − δ. J. Electrochem. Soc. *144*, L52–L53. https://doi.org/10.1149/1.1837550.

9. Andrews, J.L., Brady, M.J., McClure, E.T., and Melot, B.C. (2022). Impact of structural deformations on the performance of Li-ion insertion hosts. Chem. Mater. *34*, 4809–4820. https://doi.org/10.1021/acs.chemmater.2c00331.

10. Zhou, G., Sun, X., Li, Q.-H., Wang, X., Zhang, J.-N., Yang, W., Yu, X., Xiao, R., and Li, H. (2020). Mn ion dissolution mechanism for lithium-ion battery with LiMn2O4 cathode: in situ ultraviolet–visible spectroscopy and Ab initio molecular dynamics simulations. J. Phys. Chem. Lett. *11*, 3051–3057. https://doi.org/10.1021/acs.jpclett.0c00936.

11. Bhuvaneswari, S., Varadaraju, U.V., Gopalan, R., and Prakash, R. (2019). Structural stability and superior electrochemical performance of Sc-doped LiMn2O4 spinel as cathode for lithium ion batteries. Electrochim. Acta *301*, 342–351. https://doi.org/10.1016/j.electacta.2019.01.174.

12. Yamada, A. (1996). Lattice instability in Li(LixMn2−x)O4. J. Solid State Chem. *122*, 160–165. https://doi.org/10.1006/jssc.1996.0097.

13. Tao, Y., Lu, Y., Guo, Y., Guo, J., Xiang, M., Bai, W., Liu, X., and Bai, H. (2022). Facile synthesis and electrochemical properties of truncated octahedral Al, Ni dual doped LiMn2O4 cathode materials. J. Alloys Compd. *904*, 164027. https://doi.org/10.1016/j.jallcom.2022.164027.

14. Sun, H., Chen, Y., Xu, C., Zhu, D., and Huang, L. (2012). Electrochemical performance of rare-earth doped LiMn2O4 spinel cathode materials for Li-ion rechargeable battery. J. Solid State Electrochem. *16*, 1247–1254. https://doi.org/10.1007/s10008-011-1514-5.

15. Gu, H., Wang, G., Zhu, C., Hu, Y., Zhang, X., Wen, W., Yang, X., Wang, B., Gao, X., Zhan, X., et al. (2019). Correlating cycle performance improvement and structural alleviation in LiMn2-xMxO4 spinel cathode materials: a systematic study on the effects of metal-ion doping. Electrochim. Acta *298*, 806–817. https://doi.org/10.1016/j.electacta.2018.12.152.

16. Zhang, W., Sun, X., Tang, Y., Xia, H., Zeng, Y., Qiao, L., Zhu, Z., Lv, Z., Zhang, Y., Ge, X., et al. (2019). Lowering charge transfer barrier of LiMn2O4 via nickel surface doping to enhance Li+ intercalation kinetics at subzero temperatures. J. Am. Chem. Soc. *141*, 14038–14042. https://doi.org/10.1021/jacs.9b05531.

17. Ram, P., Gören, A., Ferdov, S., Silva, M.M., Singhal, R., Costa, C.M., Sharma, R.K., and Lanceros-Méndez, S. (2016). Improved performance of rare earth doped LiMn2O4 cathodes for lithium-ion battery applications. New J. Chem. *40*, 6244–6252. https://doi.org/10.1039/C6NJ00198J.

18. Walz, K.A., Johnson, C.S., Genthe, J., Stoiber, L.C., Zeltner, W.A., Anderson, M.A., and Thackeray, M.M. (2010). Elevated temperature cycling stability and electrochemical impedance of LiMn2O4 cathodes with nanoporous ZrO2 and TiO2 coatings. J. Power Sources *195*, 4943–4951. https://doi.org/10.1016/j.jpowsour.2010.03.007.

19. Thackeray, M.M., Johnson, C.S., Vaughey, J.T., Li, N., and Hackney, S.A. (2005). Advances in manganese-oxide 'composite' electrodes for lithium-ion batteries. J. Mater. Chem. *15*, 2257–2267. https://doi.org/10.1039/B417616M.

20. Lee, M.-J., Lee, S., Oh, P., Kim, Y., and Cho, J. (2014). High performance LiMn2O4 cathode materials grown with epitaxial layered nanostructure for Li-ion batteries. Nano Lett. *14*, 993–999. https://doi.org/10.1021/nl404430e.

21. Grechnev, G.E., Ahuja, R., Johansson, B., and Eriksson, O. (2002). Electronic structure, magnetic, and cohesive properties of ${\mathrm{Li}}_{x}{\mathrm{Mn}}_{2}{\mathrm{O}}_{4}:$Theory. Phys. Rev. B *65*, 174408. https://doi.org/10.1103/PhysRevB.65.174408.

22. Iturrondobeitia, A., Goñi, A., Lezama, L., Kim, C., Doeff, M., Cabana, J., and Rojo, T. (2014). Modification of the electrochemical activity of LiMn1.95Si0.05O4 spinel via addition of phases with different physico-chemical properties. J. Mater. Chem. *2*, 3216–3222. https://doi.org/10.1039/C3TA14793B.

23. Liu, W.-W., Wang, D., Wang, Z., Deng, J., Lau, W.-M., and Zhang, Y. (2017). Influence of magnetic ordering and Jahn–Teller distortion on the lithiation process of LiMn2O4. Phys. Chem. Chem. Phys. *19*, 6481–6486. https://doi.org/10.1039/C6CP08324B.

24. Demirel, S., Oz, E., Altin, S., Bayri, A., Altin, E., and Avci, S. (2016). Enhancement of battery performance of LiMn2O4: correlations between electrochemical and magnetic properties. RSC Adv. *6*, 43823–43831. https://doi.org/10.1039/C6RA05032H.

25. Chowki, S., Rayaprol, S., and Mohapatra, N. (2014). Antiferromagnetic super-spin freezing with partial charge and magnetic order in $LiMn_2O_4$. Mater. Res. Express *1*, 046113. https://doi.org/10.1088/2053-1591/1/4/046113.

26. Zhang, X.K., Yuan, J.J., Xie, Y.M., Yu, Y., Kuang, F.G., Yu, H.J., Zhu, X.R., and Shen, H. (2018). Phase coexistence and exchange-bias effect in $LiMn_2O_4$ nanorods. Phys. Rev. B *97*, 104405. https://doi.org/10.1103/PhysRevB.97.104405.

27. Wills, A.S., Raju, N.P., and Greedan, J.E. (1999). Low-temperature structure and magnetic properties of the spinel LiMn2O4: a frustrated antiferromagnet and cathode material. Chem. Mater. *11*, 1510–1518. https://doi.org/10.1021/cm981041l.

28. Wan, Z., Xu, Y., Sun, G., Xu, D., and Luo, X. (2022). Conflicting role of inversion of the LiMn2O4 spinel on lithium-ion battery capacity from first-principles calculations. J. Phys. Chem. C *126*, 7374–7382. https://doi.org/10.1021/acs.jpcc.2c00274.

29. Chukalkin, Y.G., Teplykh, A.E., Pirogov, A.N., and Kellerman, D.G. (2010). Magnetism of LiMn2O4 manganite in structurally ordered and disordered states. Phys. Solid State *52*, 2545–2551. https://doi.org/10.1134/S1063783410120164.

30. Kamel, M., Hanna, A.R.N., Krellner, C., Klingeler, R., Abdellah, M., Abdel-Hafiez, M., Hassen, A., Khalil, A.S.G., Abdel-Baset, T., and Hassan, A. (2021). Synthesis, optical, magnetic and thermodynamic properties of rocksalt Li1.3Nb0.3Mn0.4O2 cathode material for Li-ion batteries. Crystals *11*, 825. https://doi.org/10.3390/cryst11070825.

31. Chakrabarty, S., Jana, T.K., De, K., Das, S., Dey, K., and Chatterjee, K. (2014). Morphology dependent magnetic properties ofα-Fe_2O_3nanostructures. Mater. Res. Express *1*, 046104. https://doi.org/10.1088/2053-1591/1/4/046104.

32. Mukadam, M.D., Yusuf, S.M., Sharma, P., and Kulshreshtha, S.K. (2004). Particle size-dependent magnetic properties of γ-Fe2O3 nanoparticles. J. Magn. Magn Mater. *272–276*, 1401–1403. https://doi.org/10.1016/j.jmmm.2003.12.139.

33. Ram, P., Gören, A., Ferdov, S., Silva, M.M., Choudhary, G., Singhal, R., Costa, C.M., Sharma, R.K., and Lanceros-Méndez, S. (2017). Synthesis and improved electrochemical performance of LiMn2–xGdxO4 based cathodes. Solid State Ionics *300*, 18–25. https://doi.org/10.1016/j.ssi.2016.11.026.

34. Han, S.C., Singh, S.P., Hwang, Y.-h., Bae, E.G., Park, B.K., Sohn, K.-S., and Pyo, M. (2012). Gadolinium-doped $LiMn_2O_4$Cathodes in Li ion batteries: understanding the stabilized structure and enhanced electrochemical kinetics. J. Electrochem. Soc. *159*, A1867–A1873. https://doi.org/10.1149/2.009212jes.

35. Mohan, P., and Paruthimal Kalaignan, G. (2014). Structure and electrochemical performance of surface modified LaPO4 coated LiMn2O4 cathode materials for rechargeable lithium batteries. Ceram. Int. *40*, 1415–1421. https://doi.org/10.1016/j.ceramint.2013.07.024.

36. Vitale, S.A., Wyatt, P.W., and Hodson, C.J. (2012). Plasma-enhanced atomic layer deposition and etching of high-k gadolinium oxide. J. Vac. Sci. Technol. A *30*, 01A130–101A130. https://doi.org/10.1116/1.3664756.

37. Moulder, J.F., and Chastain, J. (1992). Handbook of X-Ray Photoelectron Spectroscopy: A Reference Book of Standard Spectra for Identification and Interpretation of XPS Data (Physical Electronics Division, Perkin-Elmer Corporation).

38. Zhang, C., Su, J., Wang, T., Yuan, K., Chen, C., Liu, S., Huang, T., Wu, J., Lu, H., and Yu, A. (2018). Significant improvement on electrochemical performance of LiMn2O4 at elevated temperature by atomic layer deposition of TiO2 nanocoating. ACS Sustain. Chem. Eng. *6*, 7890–7901. https://doi.org/10.1021/acssuschemeng.8b01081.

39. Marchini, F., Rubi, D., del Pozo, M., Williams, F.J., and Calvo, E.J. (2016). Surface chemistry and lithium-ion exchange in LiMn2O4 for the electrochemical selective extraction of LiCl from natural salt lake brines. J. Phys. Chem. C *120*, 15875–15883. https://doi.org/10.1021/acs.jpcc.5b11722.

40. Eriksson, T., Gustafsson, T., and Thomas, J.O. (2002). Surface structure of $LiMn_2O_4$ electrodes. Electrochem. Solid State Lett. *5*, A35. https://doi.org/10.1149/1.1432782.

41. Ammundsen, B., Burns, G.R., Islam, M.S., Kanoh, H., and Rozière, J. (1999). Lattice dynamics and vibrational spectra of lithium manganese oxides: a computer simulation and spectroscopic study. J. Phys. Chem. B *103*, 5175–5180. https://doi.org/10.1021/jp984398l.

42. Paolone, A., Sacchetti, A., Postorino, P., and Cantelli, R. (2005). Comment on "effect of chromium substitution on the lattice vibration of spinel lithium manganate: a new interpretation of the Raman spectrum of LiMn2O4". J. Phys. Chem. B *109*, 7587–7588. https://doi.org/10.1021/jp044931z.

43. Helan, M., Berchmans, L.J., Syamala Kumari, V.S., RaviSankar, R., and Shanmugam, V.M. (2011). Molten salt synthesis of LiGd0·01Mn1·99O4 using chloride–carbonate melt. Mater. Res. Innovat. *15*, 130–134. https://doi.org/10.1179/143307511X12998222918958.

44. Ramana, C.V., Massot, M., and Julien, C.M. (2005). XPS and Raman spectroscopic characterization of LiMn2O4 spinels. Surf. Interface Anal. *37*, 412–416. https://doi.org/10.1002/sia.2022.

45. Ouyang, C.Y., Shi, S.Q., and Lei, M.S. (2009). Jahn–Teller distortion and electronic structure of LiMn2O4. J. Alloys Compd. *474*, 370–374. https://doi.org/10.1016/j.jallcom.2008.06.123.

46. Thackeray, M.M. (1997). Manganese oxides for lithium batteries. Prog. Solid State Chem. *25*, 1–71. https://doi.org/10.1016/S0079-6786(97)81003-5.

47. Satheeshkumar, M.K., Kumar, E.R., Indhumathi, P., Srinivas, C., Deepty, M., Sathiyaraj, S., Suriyanarayanan, N., and Sastry, D.L. (2020). Structural, morphological and magnetic properties of algae/CoFe2O4 and algae/Ag-Fe-O nanocomposites and their biomedical applications. Inorg. Chem. Commun. *111*, 107578. https://doi.org/10.1016/j.inoche.2019.107578.

48. Chen, Q., Zhang, Z., and Awaga, K. (2021). Electrochemical tuning-induced magnetic transitions in geometrically frustrated spinel LixMn2O4 ($0.07 \leq x \leq 0.93$). J. Phys. Chem. C *125*, 7763–7771. https://doi.org/10.1021/acs.jpcc.1c00291.

49. Yamaura, K., Huang, Q., Zhang, L., Takada, K., Baba, Y., Nagai, T., Matsui, Y., Kosuda, K., and Takayama-Muromachi, E. (2006). Spinel-to-CaFe2O4-Type structural transformation in LiMn2O4 under high pressure. J. Am. Chem. Soc. *128*, 9448–9456. https://doi.org/10.1021/ja0612302.

50. Scivetti, I., and Teobaldi, G. (2015). (Sub) surface-Promoted disproportionation and absolute band alignment in high-power LiMn2O4 cathodes. J. Phys. Chem. C *119*, 21358–21368. https://doi.org/10.1021/acs.jpcc.5b06522.

51. Lin, Q., Lin, J., He, Y., Wang, R., and Dong, J. (2015). The structural and magnetic properties of gadolinium doped $CoFe_2O_4$ nanoferrites. J. Nanomater. *2015*, 294239. https://doi.org/10.1155/2015/294239.

52. Joshi, S., Kumar, M., Chhoker, S., Kumar, A., and Singh, M. (2017). Effect of Gd3+ substitution on structural, magnetic, dielectric and optical properties of nanocrystalline CoFe2O4. J. Magn. Magn Mater. *426*, 252–263. https://doi.org/10.1016/j.jmmm.2016.11.090.

53. Weiss, A. (1964). John B. Goodenough: magnetism and the chemical bond. Interscience publishers. New York, London 1963. 393 seiten, 89 abbildungen. Preis: DM 95 s. Ber. Bunsen Ges. Phys. Chem. *68*, 996. https://doi.org/10.1002/bbpc.19640681015.

54. Peng, Z.-d., Hu, G.-r., and Liu, Y.-x. (2005). Influence on performance and structure of spinel LiMn2O4 for lithium-ion batteries by doping rare-earth Sm. J. Cent. South Univ. Technol. *12*, 28–32. https://doi.org/10.1007/s11771-005-0366-5.

55. Puli, V.S., Adireddy, S., and Ramana, C.V. (2015). Chemical bonding and magnetic properties of gadolinium (Gd) substituted cobalt ferrite. J. Alloys Compd. *644*, 470–475. https://doi.org/10.1016/j.jallcom.2015.05.031.

56. Kresse, G., and Furthmüller, J. (1996). Efficient iterative schemes for ab initio total-energy

calculations using a plane-wave basis set. Phys. Rev. B Condens. Matter *54*, 11169–11186. https://doi.org/10.1103/PhysRevB.54.11169.

57. Kresse, G., and Furthmüller, J. (1996). Efficiency of ab-initio total energy calculations for metals and semiconductors using a plane-wave basis set. Comput. Mater. Sci. *6*, 15–50. https://doi.org/10.1016/0927-0256(96)00008-0.

58. Kresse, G., and Joubert, D. (1999). From ultrasoft pseudopotentials to the projector augmented-wave method. Phys. Rev. B *59*, 1758–1775. https://doi.org/10.1103/PhysRevB.59.1758.

59. Dudarev, S.L., Liechtenstein, A.I., Castell, M.R., Briggs, G.A.D., and Sutton, A.P. (1997). Surface states on NiO (100) and the origin of the contrast reversal in atomically resolved scanning tunneling microscope images. Phys. Rev. B *56*, 4900–4908. https://doi.org/10.1103/PhysRevB.56.4900.

60. Dudarev, S.L., Botton, G.A., Savrasov, S.Y., Humphreys, C.J., and Sutton, A.P. (1998). Electron-energy-loss spectra and the structural stability of nickel oxide: an LSDA+U study. Phys. Rev. B *57*, 1505–1509. https://doi.org/10.1103/PhysRevB.57.1505.

STAR★METHODS

KEY RESOURCES TABLE

REAGENT or RESOURCE	SOURCE	IDENTIFIER
Chemicals		
CH_3COOLi	Alfa Aeser	CAS: 867-55-0
$(CH_3COO)_2Mn$	Alfa Aeser	CAS: 6156-78-1
$(CH_3COO)_3Gd$	Alfa Aeser	CAS: 100587-93-7
2-ethylhexnoic acid	Sigma	CAS: 149-57-5
Software		
ImageJ	GitHub	https://imagej.net/
OriginLab	OriginLab Corporation	https://www.originlab.com
Other		
X-ray diffraction	Bruker	D8 Advance
phase identification	ICDD	https://www.icdd.com/
X-ray photoelectron spectroscope	Oxford Instruments	Omicron Nanotechnology
N_2 adsorption-desorption	Quantachrome	ASIQMU00U11-6
Transmission electron microscope	FEI Tecnai	G2 T20
Thermogravimetric	PerkinElmer	STA-6000
physical property measurement system (PPMS)	Quantum design	PPMS DYNACOOL
FTIR	BRUKER	VERTEX 70v
SEM	ZEISS	EVO 18

RESOURCE AVAILABILITY

Lead contact

Further information and requests for resources should be directed to and will be fulfilled by the lead contact, Rakesh Kumar Sharma (rks@iitj.ac.in).

Materials availability

This study did not generate unique reagents.

Data and code availability

All data reported in this paper will be shared by the lead contact upon request.

This article does not report original codes.

Any additional information required to reanalyse the data reported in this article is available from the lead contact on request.

EXPERIMENTAL MODEL AND SUBJECT DETAILS

Our study does not use experimental models typical in the life sciences.

METHOD DETAILS

Preparation of $LiMn_{2-x}Gd_xO_4$

In the typical synthesis procedure, the stoichiometric ratio of different precursor salts such as lithium acetate, gadolinium acetate, and manganese acetate were dissolved separately in the 2- ethyl hexanoic acid by continuous magnetic stirring at 120°C for 20 min to get a homogeneous mixing of all precursors. The temperature of the resultant precursor solution is further increased to 410°C and maintained for 8–10 h with constant stirring. A brownish powder was formed and which on calcination at 450°C for 4 h resulted

in a sample devoid of all organic impurities. Further heat-treatment at 850°C for 14 h in a box furnace, resulted in phase pure $LiMn_{2-x}Gd_xO_4$ (x = 0.00, 0.01, 0.02, 0.03 and 0.04) powder in a blackish color. The samples were named LMO, Gd01, Gd02, Gd03 and Gd04 respectively. A schematic illustration of the synthesis process is given in Scheme 1.

Sample preparation for magnetic measurements

The samples were pre-heated overnight before the analysis of magnetic properties. 20 to 50 mg of the sample was used for magnetic measurements using the PPMS instrument. ZFC and FC measurements are carried out at varied temperature conditions from 300 K to 5 K at the constant magnetic field of 200 Oe. Isothermal magnetic hysteresis analyses were measured from +5 to −5 T at constant 300K and 5K.

Computational details

DFT calculations were performed using the Vienna *ab-initio* Simulation Package (VASP).[56,57] Projector-augmented wave (PAW) potentials were employed for the ion-electron terms, with valence configurations of Li(s^1p^0), Mn(d^6s^1), Gd($4f^75d^1$) and O($2s^2p^4$), using the implementation of Kresse and Joubert.[58] Hubbard U_{eff} corrections were modelled by considering the on-site Coulomb corrections of Mn 3*d* and Gd 4f orbitals using the spin-polarized GGA + U method introduced by Dudarev et al.[59,60]; U_{eff} was set to 4.84 and 6.0 eV for Mn and Gd atoms respectively. The number of VASP plane waves was controlled by the cut-off energy, which we set to 550 eV, having tested for cut-off convergence. Brillouin-zone integrations were performed during geometry relaxation using k-point grids with a 4 × 4×4 for pure $LiMn_2O_4$ and the doped structures $LiMn_{2-x}Gd_xO_4$.

QUANTIFICATION AND STATISTICAL ANALYSIS

Particle size of the samples is calculated from the SEM image (Figure 3) as mean average using IMAGE J software and no other statistical analysis and quantifications used.

ADDITIONAL RESOURCES

There are no additional resources need to be declared in this manuscript, additional requests for this can be made by contacting the lead contact.